Iceland Liechtenstein Norway grants

Executive Agency for Higher Education, Research, Development and Innovation Funding

Short annual reporting

2021

Promotor-PP:

According to the workplan of the ElastoMETA project, PP was supposed to implement in 2021 the following activities: Activity A3.2 Optimization of UV-NIL fabrication; A3.3 Structural characterization of the UV-NIL optimized metasurfaces; A3.4 First "UV-NIL" source and lens characterization for sensor detection; Act. 3.5 Elastomeric embedding documentation and processes.

The work of the PP partner can be summarized as follows:

- The PP have used different recipes for UV-NIL and Stamp fabrication;
- Have attended various webinars (see the overview connected with the deliverables) and acquire two equipments in order to improve the process;
- Have contacted the EVG (vendor of the NIL equipment) in order to optimize the fabrication process;
- Have made preliminary measurements of the lenses and send the viable ones to partner P1 for better analysis;
- Have made multiple SEM characterizations of the structures;
- Have made FTIR, wettability, optical imagines and AFM measurements of the lenses;
- Study the literature for the best elastomer for the embedding process;
- Have made trials for the embedding with Sylgard 184.

Various SEM micrograohs were aquired in order to discover the differences between the simulated and fabricated structures.

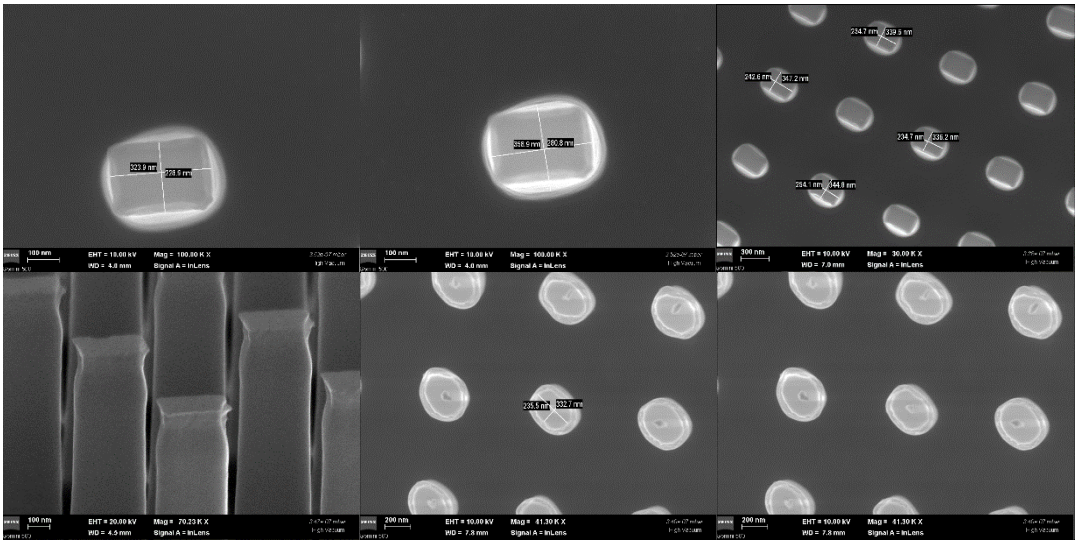

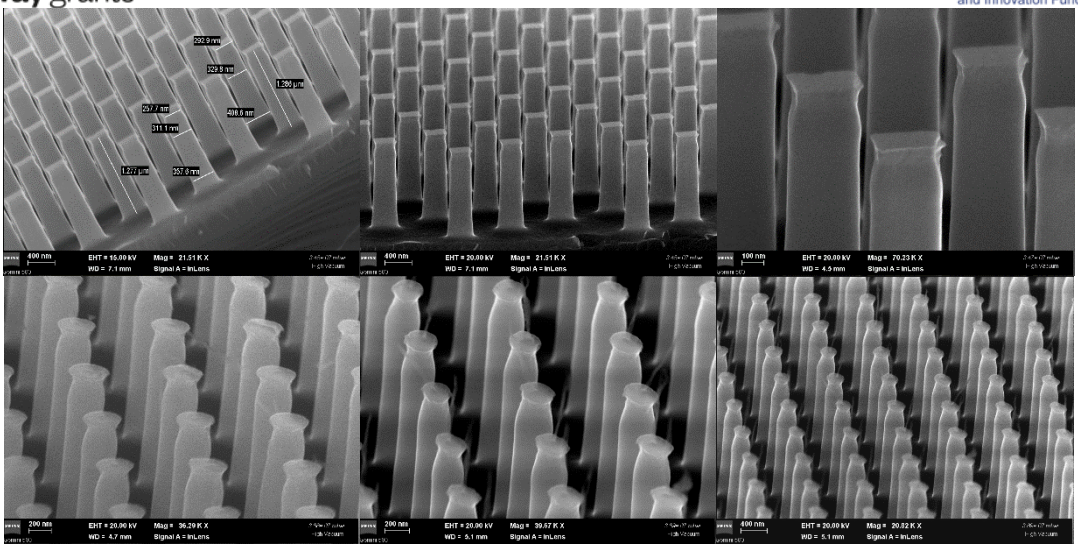

Figure 1. SEM micrografs of the metalens patterns made by EBL and NIL

The values of the patterns that forms lens with measureable efficiencies are indexed in the folowing table.

Table 1: Dimensions of the metalenses patterns.

Sample	Dimensions			Deviation from target		
	Height-h (µm)	Width-w (nm)	Length-l (nm)	Height (%)	Width (%)	Length (%)
Target	1200	230	354	-	-	-
EBL metalens	1200	236.8	355.2	0	-2.96	-0.33
Stamp 1	1083	224,2	340,4	9.75	2.52	3.84
UV-NIL metalens 1	842	235.9	312.6	29.83	-2.57	11.19
UV-NIL metalens 2	1066	210.3	302.6	11.16	8.56	14.52
UV-NIL metalens 3	1280	247.2	307	-6.66	-7.48	13.27

The quality of the stamps were analised also by SEM imaging:

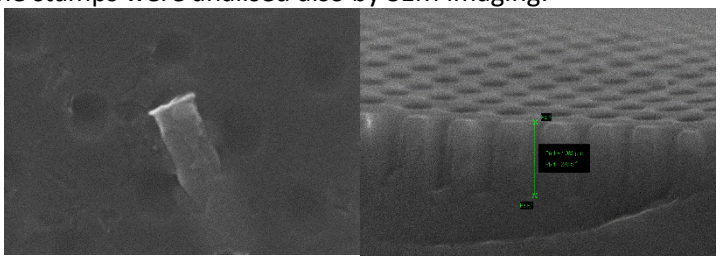

Figure 2. SEM pictures of the PDMS stamp

For the stamp realized by successive UV irradiation, the SEM analysis reveal that the UV-PDMS polymer was partially capable to produce the inverted copy of the metalenses from the fabricated master. The shape of the holes is looking more oval than rectangular, probably due to the fact that the successive curing time before delamination from Si master was too short and thus the cavities have suffered deformation on the direction of the stamp detachment. The high of the holes measured after the thin gold layer deposition was 1.083 µm with the l = 340,4 nm and w = 224,2 nm. Thus, the deviation from the master is almost of 4.2% in the length and 5.3% in the width. More, in this case it seems that at the demolding of the stamp from the master step, due to the adhesion forces between them and due to the geometry of the pillars pattern fracture occurs that further remains in the stamp

silicone rubber affecting the nanoimprint results, although the Si master was treated with ASL. As a consequence, the use of the master to fabricate other stamps is compromised.

The optical and AFM images are reveling the distribution of the patterns and the top view of the lens, as can be seen in Figure 3.

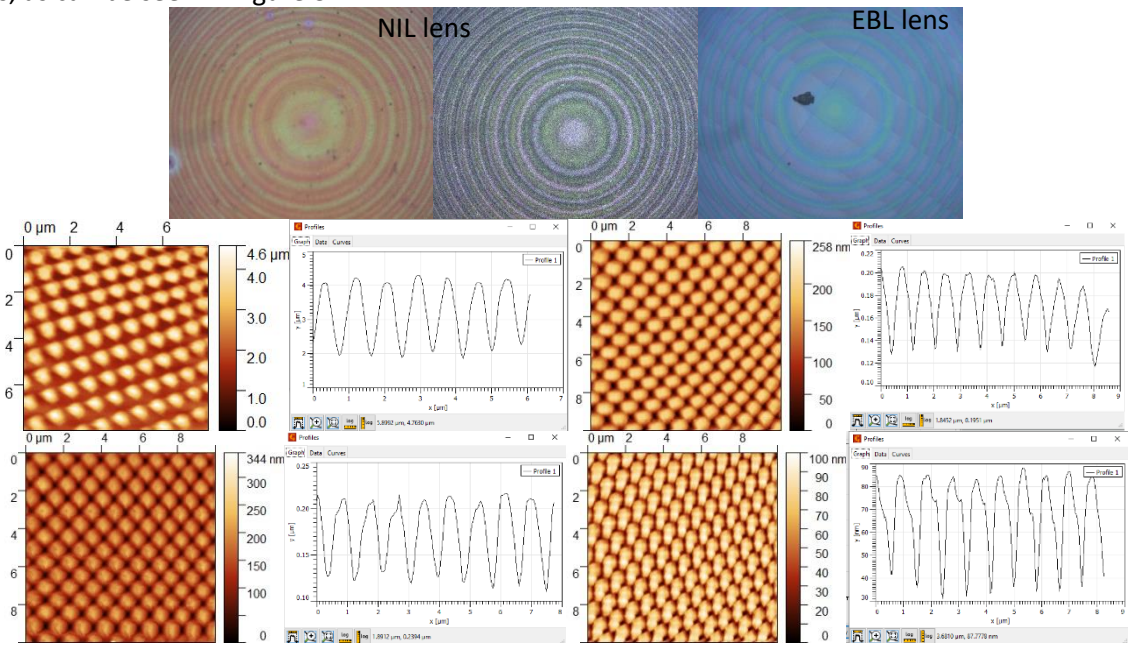

Figure 3. AFM images of the lenses obtained by UV-NIL method

For the embedding part (Act A 3.5) one of the first results obtained are more suggestive expressed by the following Figure 4, unfortunately due to the sensitivity of the elastomer we couldn't make other analysis on the samples.

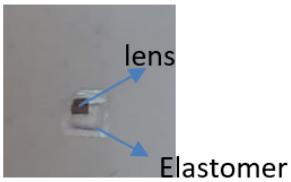

Figure 4. Image of the lens embedded in the elastomer- Sylgard 184

SINTEF- P1:

According to the workplan of 2021, P1 was involved in two activities: Act. 3.1: A theoretical study of the interaction between the unit cells of different geometry or rotation aims to help in the design of subunit structures for efficient metasurfaces and Act 3.4: UV-NIL" source and lens characterization for sensor detection-helping the CO partner.

The work of the partner can be divided in:

Simulation work:

- For the Bosch structures have been test the hypothesis that rounding in the grooves leads to a fall in cross-polarization efficiency.
- For the NIL samples made by PP have performed simulations of the efficiency according to the pillar's dimensions.
- Also, simulations regarding the influence of the tapered walls on the lens efficiency.

- Simulated by the Finited Difference Time Domain (FDTD) method the case in which instead of a rectangular shape the pillars have an oval shape.

Optical characterization work:

- Have worked to further develop and improve the optical measurement apparatus and assist the project promoter with their setup.
- Optical measurements on metalenses that we fabricated last year on 4-inch SOI wafers and etched by P2 and compare them with our results obtained on the samples etched applying Bosch method.
- SEM micrographs of the SOI samples etched by P2.
- Optical measurements on metalenses fabricated by PP: We received samples from the PP-partner and measured them to attain efficiencies that corresponded well with the simulations and their target efficiency.

In order to explain the low efficiency for the NIL metalenses we simulated by the Finited Difference Time Domain (FDTD) method the case in which instead of a rectangular shape (Figure 5– dashed line) the pillars have an oval shape. The first simulation parameters for the ellipse, were for the target dimension (w = 2 × a = 230 nm; l = 2 × b = 354 nm) showing that even when the cross-section of the pillars is not perfectly rectangular the efficiency should be near the theoretical one (Figure 5- black continuous line). The low efficiency of the UV-NIL metalens is given, according to the simulations (Figure 5 – green line), by the nearly round shape of the pillars, which imply a decrease in the cross-polarization efficiency.

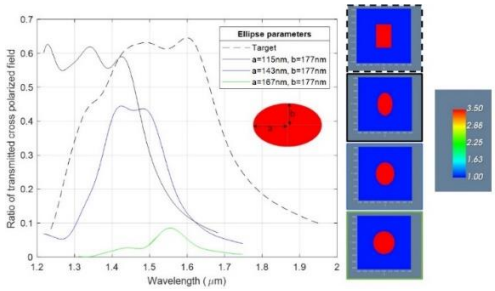

Figure 5. *Plots of ellipse simulation curves, with different values for the a and b parameters based on metalenses patterns dimensions found from SEM images.*

In the case of the EBL metalenses, the decrease in the efficiency (from the theoretical 60% to 45%), can be given by the pillars shape characterized by: (i) a small rectangular "hat " on top followed by a short neck and after going down with rounded corners similar with the simulation highlighted by the blue continuous line (Figure 5) and (ii) slightly tapered profile. According to the simulations (see Figure 6) the tapered profile can induce a further decrease of the transmittivity and therefore a decrease in the lens efficiency. One way to improve the efficiency, of both EBL and NIL metalenses, to a value above 95% is to change the silicon substrate with a quartz one.

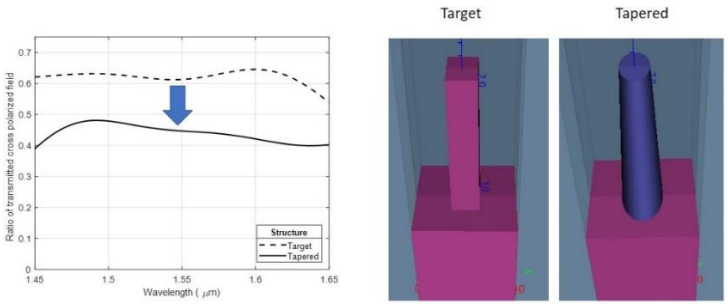

Figure 6*: Plots of simulation curves considering the cases in which the patterns presents straight (target) or tapered profile*

Regarding the *optical measurements* the results are:

(A) The measured lens efficiencies of resulting dimensions of Bosch 2 are shown in Figure 7b. A simulation curve is added for a rectangular structure with elliptical washboard surface patterns intended to mimic the structures as seen in SEM images. While the wavelength for peak optical efficiency coincides well with the measurements, the measured efficiency is somewhat lower than predicted. The geometry of the pillar is however not easily simulated accurately. Also, these pillars were not properly stripped for resist and etch polymer prior to optical testing, although this is at least partially accounted for in simulation. Despite their potentially being several sources of error with the simulations, a part of the discrepancy is possibly explained by rounding effects within the groves of the washboard patterns, where it seems possible that the pillar cross-section ceases to be rectangular and rather begins to become more circular. Circular cross-sections are incapable of converting between circular polarization states, hence reducing the efficiency of the metasurface. Despite the drawbacks of the resulting structures in the Bosch 2 fabrication, it is worth noting that the optical performance is comparable to that achieved by the Cryo process (Figure 7a).

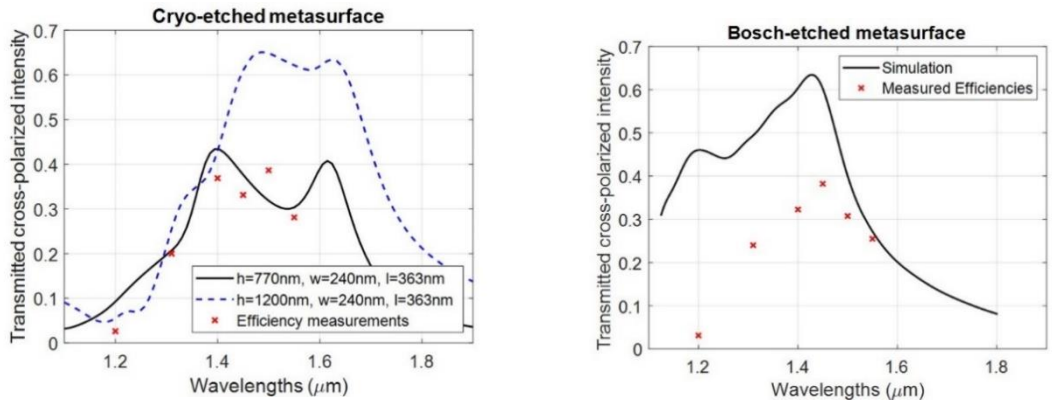

(a) (b)

Figure 7. Plots of simulation curves based on dimensions found from SEM images and datapoints from efficiency measurements. (a) Results for cryo-etched metasurface. Using the Rigorously Coupled Wave Analysis (RCWA) simulation method for a pillar of dimensions h=770 nm, w=240 nm, l=363 nm and p=835 nm gives a transmission curve (solid curve) which fits qualitatively with the measured efficiency of the cryo-etched metasurface. Increasing the height in the simulations to the target value of h=1200 nm reveals that the lens efficiencies are raised to the design efficiency of the target structure. This indicates that a longer etch would have yielded a higher efficiency. (b) Results of the second Bosch run .

(B) A number of four metalenses fabricated using EBL as well as using NIL, two for each technique, were optically characterized and their focal spot profiles being shown in Figure 8. Since respectively both EBL metalenses and both UV-NIL metalenses were identical from the focal spot and efficiency point of view, we chose to represent just one for each type.

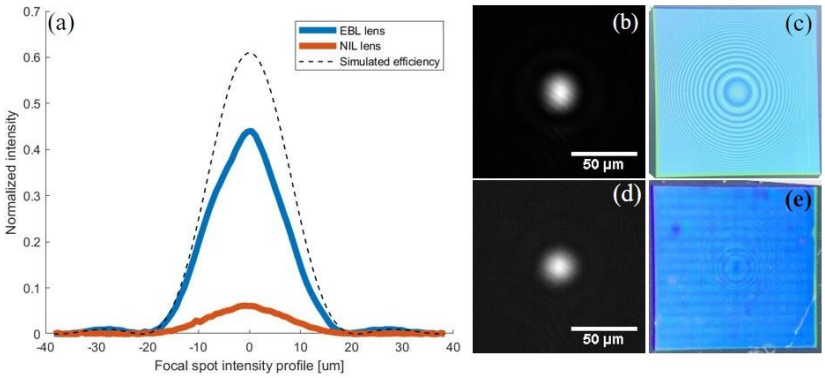

Figure 8. (a) Focal spot intensity profile of a metalens made using EBL (blue) and a metalens made using NIL (orange), compared to the theoretical profile for a lens with the designed efficiency (dashed line) for 1550 nm laser light. As discussed in Sect. 2.1. the less than unity efficiency is largely attributed to using a silicon substrate. (b) Image of the focal spot from the EBL lens (c) Optical microscope image of the EBL lens (d) Image of the focal spot of the NIL lens, for 1550 nm laser light. (e) Optical microscope image of the NIL lens with side lengths 1.5 mm. Note that for the focal spot measurements a circular 900 µm aperture is placed in front of the lenses.

The focal spot profiles are compared to that of an antireflection coated aspherical lens, and the efficiencies are found to be 45% for the metalenses made directly using EBL, and 6% for the metalenses made using NIL. These efficiency numbers do not include the 31% reflection loss from the backside of the Si substrate. As can be seen in Figure 8, all lenses have the same diffraction limited spot profile which is a result of the geometric phase design – the phase of the cross polarized light being decided by the nanostructure orientation, which is accurately reproduced in both the EBL and NIL processes.

Meanwhile, the focusing efficiency is dependent on the length and width of the nanostructures (see Table 1). When achieving the target dimensions, we would expect on the order of 60 % efficiency from simulations. However, the analyzed lenses fabricated using NIL, having reached the target high dimensions but round top and visible surface defects have low cross-polarization efficiency, therefore the fabrication process has to be optimized for better structure uniformity as well as for achieving final dimensions closer to the target ones – for example, by taking systematic fabrication errors into account in the design process.

IMT-P2:

According to the workplan of 2021, P2 was involved in two experimental activities: Act. 3.2 and Act. 3.5 -Reactive Ion Etching of the structures obtained by UV-NIL.

Summarizing P2:

- Have done supplementary optimization of the EBL and DRIE processes.
- Have done the removal of the residual layer and the dry etching process.
- Have acquired optical and SEM images during the fabrication's steps.
- Have supplied the masters for PP for the embedding experimental part of the project.

The following paragraphs will briefly present the main results obtained for each activity.

(a) The first etching processes were performed on 4 inches SOI (Silicon on Insulator) wafers, having the following specifications: CZ growth method; buried oxide layer thickness of 0.5 µm; 30 µm handle wafer thickness; type N (Phosphorus); orientation <100>; thickness 430 µm.

By using this substrate, the lens' layout (presented in the previous report: rectangular pillars with width × length of 235 × 355 nm) was transferred onto the SOI wafers using UV-NIL patterning method. The EBL patterning was performed at IMT-Bucharest, by P2, while the UV-NIL process was done at SINTEF MiNaLab, by P1. The wafers patterned by EBL used a thin film of 20 nm of Ti as masking layer for the following etching process, while the UV-NIL patterned wafers had a mr-NIL 210 resist with a thickness of 150 nm.

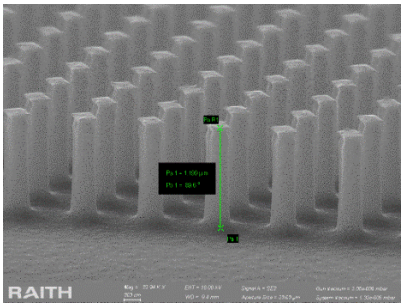

Figure 9. Cross-sectional view of SEM image of the nanopatterned silicon after cryogenic etching process (wafer processed by EBL technique).

Vertical sidewalls, smooth etched surface and heights of around 1200 nm were observed. In order to transfer the pattern from the mr-NIL210-200 nm resist (patterned by UV-NIL) to the silicon wafer, it was first required to remove the residual layer (RL—the resist formed between imprinted pillars). This process was performed by oxygen plasma, using an RIE system (Etchlab SI 220-Sentech Instruments, Berlin, Germany). Due to the significant non-uniformity thickness of the residual layer between wafers, oxygen etching was performed in subsequent steps, with optical investigations in between (Figure 10), which allowed us to evaluate the total required etching time.

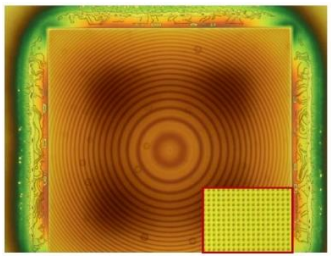

Figure 10. Optical microscopy image of the metalens after 30 s. of oxygen plasma (during the RL removing process)

The subsequent etching of the silicon wafers was achieved by using the same cryogenic process presented above for the etching of structures processed by EBL. Figure 11 presents silicon pillars achieved using a 50 sec. process of the residual layer removal (O_2 plasma-RIE process) and a 43 sec. process for the DRIE etching of the silicon (Cryogenic DRIE process).

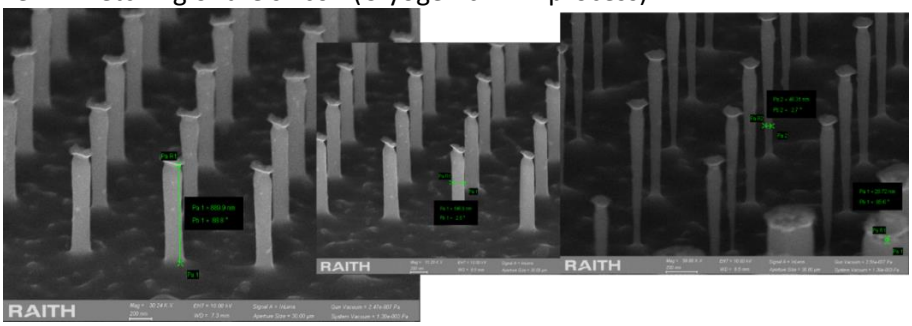

Figure 11. Cross-sectional view of SEM images of the nanopatterned silicon after 50 sec. O_2 plasma-RIE process and 43 sec. Cryogenic DRIE process.

It can be seen that the obtained etching depth was around 800 nm, the etched surface was rough and the silicon pillars were overetched at the bottom. These features can be explained that after 50 sec. of O_2 plasma-RIE process, there remained a thin film of residual layer that acted as a masking layer to DRIE etching process. Therefore, the etching depth was only 800 nm, instead of 1200 nm.

Three more wafers were processed using longer O_2 plasma-RIE process: two with 60 sec., and one with 70 sec. Figure 12 shows the patterned metalens obtained after 60 sec. of oxygen plasma process and 43 sec. cryogenic DRIE process. After performing the process of removing the residual

layer using O_2 plasma, several resist bubbles appeared, and after performing the cryogenic process, they became more pronounced.

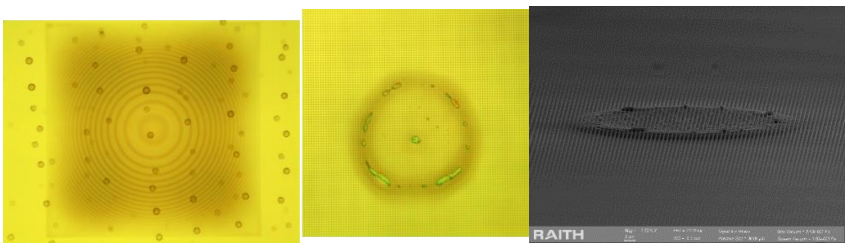

Figure 12. The patterned metalens: (a) Optical microscopy images of the structure after 60 s. of oxygen plasma and (b) SEM image of the nanopatterned silicon after 43 sec. of cryogenic DRIE process.

The obtained etching depth was around 1200 nm, but the etching process was nonuniform due to the resist bubbles.

The last two wafers were processed using shorter times for the process of removing the residual layer: 30 sec. and 35 sec., respectively. The etching of the Si pillars was performed using the 43 sec. of cryogenic DRIE process. These wafers were cut into chips and sent to the P1 partner in order to measure the efficiency of the fabricated lenses. The SEM images of the nanopatterned silicon, pointed out in Figure 13, showed an etching depth of around 800 nm.

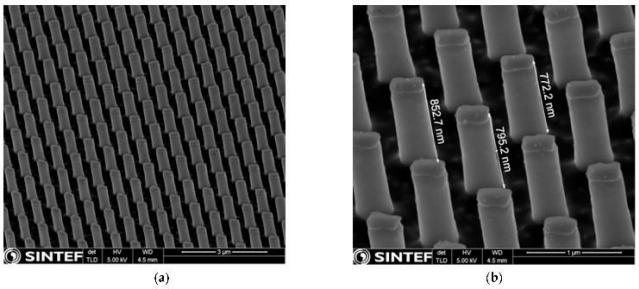

Figure 13. Cross-sectional view of SEM images of the nanopatterned silicon after cryogenic etching process (tilt 45°)—(a) the fidelity of the nanopillars (b) with corresponding measured heights.

UB-P3:

According to the workplan of the ElastoMETA project, P3 was supposed to implement in 2021 the following activity: Act. 3.1: A theoretical study of the interaction between the unit cells of different geometry or rotation aims to help in the design of subunit structures for efficient metasurfaces.

Therefore, the work has been divided in both theoretical and numeric simulations starting from the point that there are several types of aberrations which are significant for the operation of metalenses, the most commonly encountered being the chromatic, spherical and coma aberrations. However, since a metalens always discretizes the transmitted/reflected phase, being composed of a certain number of meta-atoms, the aberrations induced by phase discretization must also be accounted for. This last source of aberrations was neglected up to now. Because in usual applications the light sources are narrowband, we have not considered chromatic aberrations; anyway, several methods to minimize them are known, such as, for instance, using metalenses doublets [1,2], multilayer metasurfaces [3] or highly anisotropic meta-atoms [4,5]. In this context it should also be mentioned that spherical and coma aberrations of metalenses can be corrected by aplanatic metasurfaces [6] or well-designed doublet metalenses [1].

While, in general, the estimation of aberrations is performed using geometric ray tracing [7-9], assigning specific aberration types to different Zernike polynomials [10] or assuming a certain expression of the phase distribution imparted by the metalens on an incoming optical field [11,12],

their effect is to modify the beam shape in the focal plane of the metalens. Thus, a wave-optic approach is needed to describe the influence of aberrations, irrespective of their type, on the performance of metalenses. Our analysis was based on the fact that the shape of single-peaked intensity distributions $I(x,z)$ can be quantitatively characterized by intensity-defined moments that determine

- the average position of the intensity distribution along the transverse *x* and longitudinal *z* axes, defined as

$$\xi_{av} = \langle \xi \rangle = \int \xi I(\xi) d\xi \,/ \int I(\xi) d\xi \,, \quad \xi = x, z$$

- the spatial extent of the intensity distribution along the *x* and *z* axes, defined via the second-order moment of the intensity as [13]

$$\Delta\xi = 4\sqrt{\langle \xi^2 \rangle} = 4 \sqrt{\int (\xi - \xi_{av})^2 I(\xi) d\xi \,/ \int I(\xi) d\xi \,}, \quad \xi = x, z$$

- the shape of the intensity distribution along the *x* and *z* axes, parameterized via the skweness *S* and kurtosis *K* coefficients defined as:

$$S_\xi = \langle \xi^3 \rangle / \langle \xi^2 \rangle^{3/2}, \qquad K_\xi = \langle \xi^4 \rangle / \langle \xi^2 \rangle^2, \quad \xi = x, z$$

with $\langle \xi^m \rangle = \int (\xi - \xi_{av})^m I(\xi) d\xi \,/ \int I(\xi) d\xi$, *m* = 3, 4. The skewness quantifies the (lack of) symmetry of a distribution, negative (positive) *S* values indicating single-peaked distributions that have a longer left (right) tail, while *S* = 0 corresponds to a symmetric distribution to the left and right. The kurtosis *K* evaluates the relative size of tails of a single-peaked distribution with respect to a normal, Gaussian function, for which *K* = 3 (and *S* = 0). Thus, *K* values higher (lower) than 3 indicate distributions that have heavy (light) tails with respect to a Gaussian. The parameters S and K are employed to distinguish the shape of statistical distributions in wide areas of research: in medical imaging [14,15], material science [16], observational cosmology [17], optics [18,19], etc.

Whether defined for single-peaked distributions, when appropriately defined, the above-defined parameters can be also used to characterize the shape of diffracted multi-peaked/rippled optical fields that have pronounced dominant maxima on both transverse and longitudinal directions. In particular, these parameters can describe the optical field in the focal plane of a metalens and the effect of associated aberrations on the focusing performances.

In the following we keep our analysis general, in the sense that we do not refer to a particular metalens, but consider an arbitrary diffracting surface consisting of a discrete number *N* of meta-atoms with dimension Λ along the *x* axis that impart a precisely controllable phase $\phi_m(x)$ on an incident light field, such that the metalens approximates in a reasonable way the ideal, continuous hyperbolic phase distribution $\phi_{id}(x) = (2\pi/\lambda)[f - \sqrt{x^2 + f^2}]$ of a focusing element with focal length *f*; for a hyperbolic phase profile there are no spherical aberrations for axially incident fields. Note that, for simplicity, we considered a two-dimensional intensity profile $I(x,z)$, which can represent either the light intensity distribution of a radially symmetric metalens in a longitudinal plane or of a cylindrical metalens. We also assume that the transmission coefficient of the metalens is the same across its surface. The metalens was studied under axial and off-axis illumination, conditions under which discretization aberration only and, respectively, spherical, coma and discretization aberrations can occur.

The dimension of the metalens $D = N\Lambda$ is considered to be defined by an opaque aperture and the meta-atoms are assumed anisotropic, so that they can rotate with an azimuthal angle α in the

metalens plane (see the inset of Fig. 14). We assume in the following that α does not change continuously from one unit cell to the other, but in steps of $\Delta\alpha$, the corresponding phase imparted by unit cells being allowed to vary in steps of $\Delta\phi_m$. The values of $\Delta\alpha$ (and thus of $\Delta\phi_m$) are chosen by design; for smaller values of this parameter, the ideal phase profile is reproduced better, but the complexity in the fabrication of metalenses is increased. Figure 14 represents the ideal (black line) and step-like approximations of the phase distribution of a lens with a focal distance of f = 10 mm when $\Delta\phi_m$ is 10° (red line) and 20° (blue line), if λ = 1.3 μm, Λ = 450 nm and $N/2$ = 400; part of the figure is enlarged for better visualization of all curves. These values for f, λ and Λ will be used throughout this study.

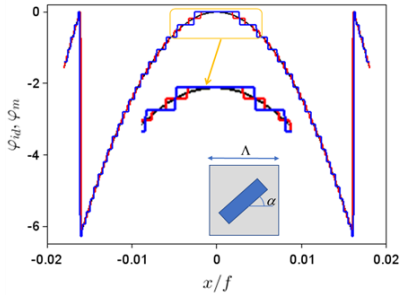

Fig. 14

If the metalens is illuminated by a normalized collimated optical E_0 = 1, incident at an angle θ with respect to the z axis, the field immediately after the metalens, situated at z = 0, is $E(x, z = 0) = E_0\exp(i2\pi\theta x/\lambda)\exp[i\phi_m(x)]$ assuming that the transmittance equals 1. The spatial distributions of the absolute value of the electric fields after the metalens for the normal/ axial, i.e. θ = 0, and tilted incidence cases are illustrated in Fig. 15(a) and, respectively, Fig. 15(b). All spatial coordinates are normalized to the focal length f of the metalens. We have calculated the electric field profile for $z > 0$ applying the diffraction integral in the Fresnel approximation to the discontinuous optical field $E(x, z = 0)$.

These figures show that the field distributions are not single-peaked. In particular, in the axial illumination case, the spatial field distributions along the longitudinal z axis (for x = 0), as well as along the transverse direction at the focal point (the x-distribution of the intensity at the z coordinate at which the absolute value of the z-dependent field is maximum) represented in Figs.15(c) and 15(d), respectively, although displaying a dominant maximum near the focal point of the perfect lens, show a multi-modal structure, with pronounced ripples along x. These ripples affect especially the S and K values (and not so much the average positions and spatial extents) so that, in order to obtain intensity-based moments pertaining only to the main peak of the field distribution along x, we have first determined x_{av} and Δx taking into account absolute values of the electric field higher than 1/40 of the peak value, and then calculated S and K considering only the electric fields with absolute values in an interval of $5\Delta x$ centered around x_{av}. As can be seen from the inset of Fig. 15(c), where the relevant region for $N/2$ = 600 (the red curve) is highlighted by two (also) red vertical lines, this interval is broad enough to account for the tail of the field intensity. No such precautions were needed for calculating the intensity-based moments along the z axis, since the field distribution is significantly less rippled, but in this case we had to subtract the background (equal to 1) from the electric field absolute values in order to obtain meaningful results (see Fig. 15(d)).

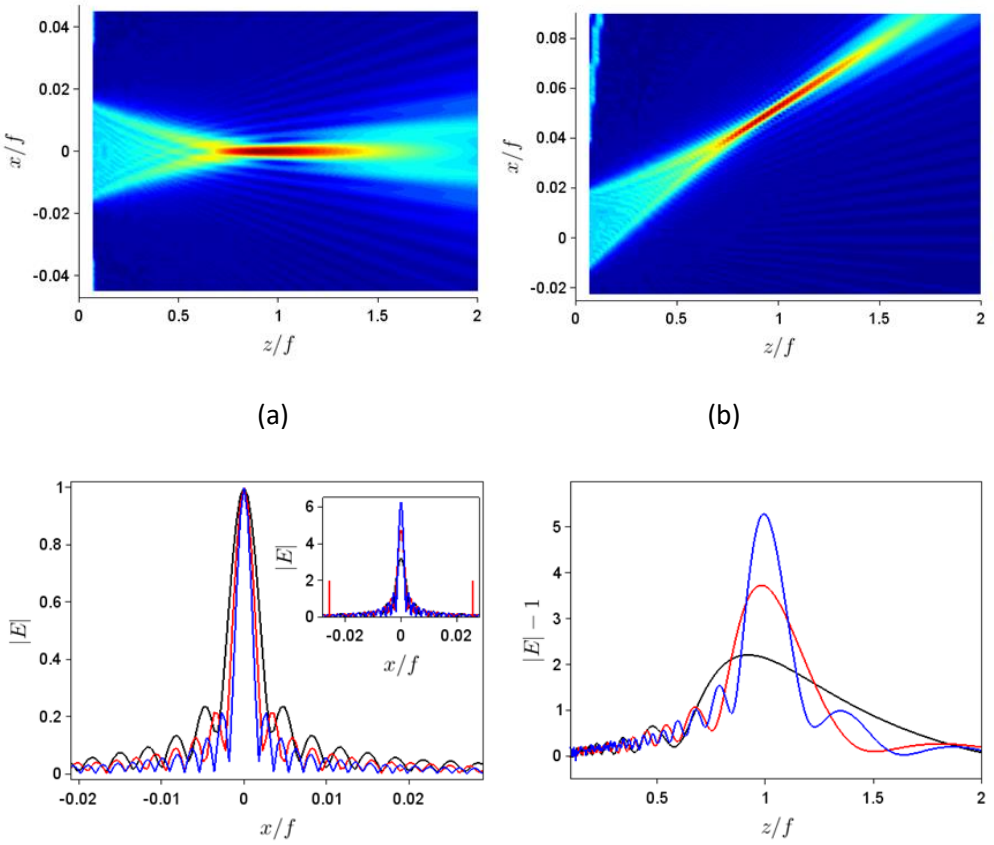

Fig. 15

Numerical simulations results

To understand why the behavior of all intensity-based moments at large tilting angle changes dramatically, especially for larger aperture sizes, we have plotted the spatial distribution of the absolute field values in this case (see Fig. 16 (a)) and have discovered that, besides the propagation direction imposed by the tilting angle, constructive interferences appear along other directions, such that we have no longer one propagating beam but several. Figures 16(b) and 16(c) show the transversal and longitudinal, respectively, field distributions in this case for $\Delta\phi_m$ = 30° and $N/2$ = 400 (black line), 600 (red line) and 800 (blue line). A second transverse peak is clearly visible in this case for the largest aperture size. The z-distribution of the field has no longer one obvious maximum for larger apertures, but several, in agreement with the simulations in Fig. 16(a). Again, the change in beam shape, especially significant at high tilt angles and high apertures, is well described by S_x, K_x, S_z and K_z, whereas the appearance of additional beams propagating at other angles has a pronounced effect also on the spatial extent and average position values along both x and z. Note that, at least for tilting illumination angles below 5°, the values of skewness and kurtosis parameters are comparable with the values for axial illumination, which shows that phase-discretization-induced aberrations are still the predominant cause of beam shape changes/low performance of metalenses.

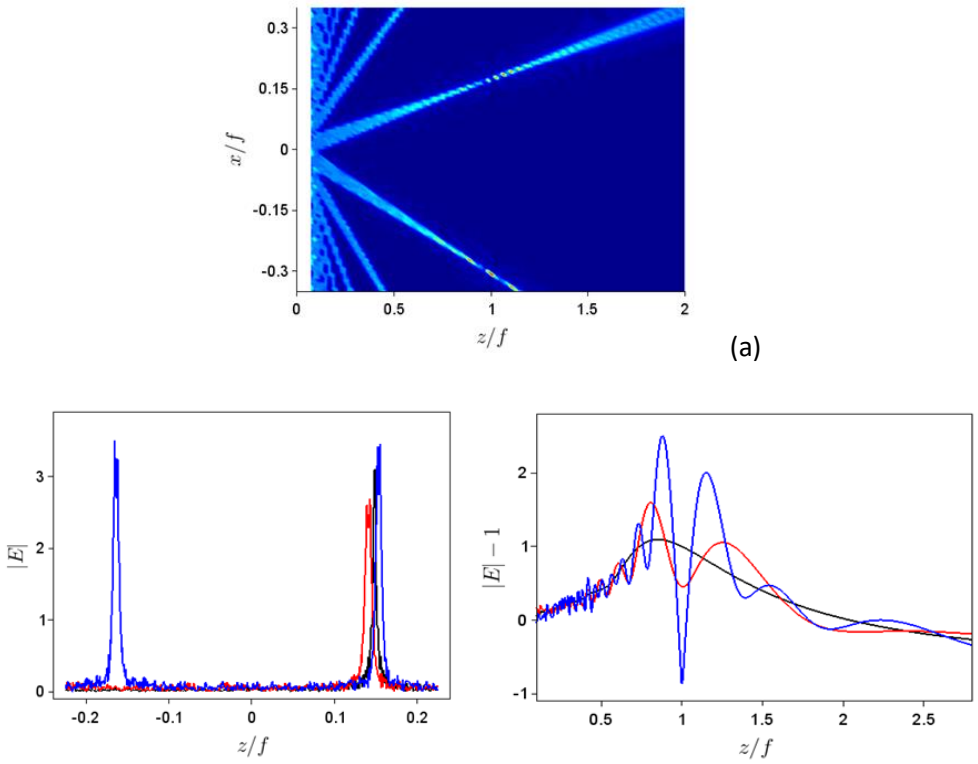

Fig.16

References

1. C. Kim, S.-J. Kim, B. Lee, Opt. Express 28, 18059-18076, 2020; **2**. B. Groever, W.T. Chen, F. Capasso, Nano Lett. 17, 4902-4907, 2017; **3.** Y. Zhou, I.I. Kravchenko, H. Wang, J.R. Nolen, G. Gu, J. Valentine, Nano Lett. 18, 7529-7537, 2018 ; **4.** W.T. Chen, A.Y. Zhu, V. Sanjeev, M. Khorasaninejad, Z. Shi, E. Lee, F. Capasso, Nat. Nanotechnol. 13, 220-226, 2018; **5.** W.T. Chen, A.Y. Zhu, J. Sisler, Z. Bharwani, F. Capasso, Nat. Commun. 10, 355, 2019; **6.** F. Aieta, P. Genevet, M. Kats, F. Capasso, Opt. Express 21, 31530-31539, 2013; **7.** P.D. Lin, R.B. Johnson, Opt. Express 27, 19712-19725, 2019; **8.** R.G. Gonzalez-Acuña, M. Avendaño-Alejo, J.C. Gutiérrez-Vega, J. Opt. Soc. Am. A 36, 925-929, 2019; **9.** J. Sasian, Appl. Opt. 59, G24-G32, 2020; **10.** Z. Wang, O. Baladron-Zorita, C. Hellmann, F. Wyrowski, Opt. Express 28, 24459-24470, 2020; **11.** S.-W. Moon, Y. Kim, G. Yoon, J. Rho, iScience 23, 101877, 2020; **12.** H. Liang, A. Martins, B.-H.V. Borges, J. Zhou, E.R. Martins, J. Li, T.F. Krauss, Optica 6, 1461-1470, 2019; **13.** M.A. Porras, R. Medina, Appl. Opt. 34, 8247-8251, 1995; **14.** A. Anand, I. Moon, B. Javidi, Proc. IEEE 105, 924-946, 2017; **15.** B. Javidi, A. Mark, Opt. Express 26, 13614-13627, 2018; **16.** T.R. Thomas, Precision Eng. 3, 97-104, 1981; **17.** A. Ben-David, S. von Hausegger, A.D. Jackson, J. Cosmol. Astropart. Phys. 11, 019, 2015; **18.** D. Dragoman, R. Tudor, J. Mod. Opt. 64, 2328-2335, 2017;19. D. Dragoman, Prog. Opt. 37, 1-56, 1997.